

First CH₃D detection in Class 0/I proto-brown dwarfs: constraints on CH₄ abundances

Riaz, B.¹* & Thi, W.-F.²

¹ *Universitäts-Sternwarte München, Ludwig Maximilians Universität, Scheinerstraße 1, 81679 München, Germany*

² *Max-Planck-Institut für Extraterrestrische Physik, Giessenbachstrasse 1, 85748 Garching, Germany*

Accepted 2022 January 18. Received 2022 January 17; in original form 2021 November 11

ABSTRACT

We report the first detection in the $J_K = 1_0 - 0_0$ rotational transition line of CH₃D towards three Class 0/I proto-brown dwarfs (proto-BDs) from IRAM 30 m observations. Assuming a rotational temperature of 25 K, the CH₃D abundances (relative to H₂) are in the range of $(2.3\text{--}14.5) \times 10^{-7}$. The CH₄ abundances derived from the CH₃D abundances and assuming the DCO⁺/HCO⁺ ratios are in the range of $(0.05\text{--}4.8) \times 10^{-5}$. The gas-phase formation of CH₃D via CH₂D⁺ is enhanced at high densities of $10^8\text{--}10^{10}$ cm⁻³ and our observations are likely probing the innermost dense and warm regions in proto-BDs. Thermal and/or non-thermal desorption can return the CH₃D and CH₄ molecules formed at an early stage on grain surfaces to the gas-phase. The gas phase abundances are indicative of warm carbon-chain chemistry in proto-BDs where carbon-chain molecules are synthesised in a lukewarm ($\sim 20\text{--}30$ K) region close to the central source.

Key words:

(stars:) brown dwarfs – stars: formation – stars: evolution – astrochemistry – ISM: abundances – ISM: molecules – stars: individual: ISO-OPH 200

1 INTRODUCTION

Methane (CH₄) has been fundamental in determining the properties of the coldest compact astrophysical sources, the T- and Y-type brown dwarfs (e.g., Cushing et al. 2011; Kirkpatrick et al. 2012). Their temperatures range between a few hundred kelvin and a few thousand kelvin, with most of their energy emitted at the infrared wavelengths. At these temperatures, brown dwarfs present strong methane absorption in their atmospheres, which is best probed by observing the CH₄ rovibrational spectrum in the near-infrared, most notably the fundamental absorption bands near ~ 1.58 μm and ~ 3.3 μm . The presence and strength of near-infrared methane absorption in their atmospheres has been a key feature for the identification and classification of large numbers of Y- and T-type brown dwarfs.

Similar observations are difficult for early-stage Class 0/I proto-brown dwarfs (hereafter; proto-BDs) due to the high extinction and the excess continuum emission from the circumstellar material in the infrared that does not allow observing these photospheric CH₄ bands (e.g., Riaz & Bally 2021). Also, CH₄ does not have a pure rotational spectrum. The kinetic temperatures found in the cold, dense gas typical of molecular clouds and embedded Class 0/I cores are too low ($\sim 10\text{--}100$ K) for the vibrational excitation of interstellar molecules, which makes it difficult to observe the infrared CH₄ bands under such conditions. Absorption study of near-IR CH₄ lines towards HL Tau was unsuccessful with a 3σ upper limit CH₄/CO ratio of 0.02% (Gibb et al. 2004).

An alternative method to indirectly obtain methane abundance measurements is by observing its singly deuterated form, or mono-deuterated methane (CH₃D). CH₃D has a pure rotational spectrum and a non-zero small dipole moment (0.0057 Debye), which makes it possible to observe the CH₃D rotational transitions from the ground (e.g., Womack et al. 1996).

We report here the first detection in the $J_K = 1_0\text{--}0_0$ rotational transition line of CH₃D at millimeter wavelength of 232.6 GHz towards early-stage Class 0/I proto-BDs. In addition to CH₃D abundance, we have obtained an estimate on the CH₄ abundance by adopting the molecular DCO⁺/HCO⁺ ratios. It is interesting to investigate how much of the CH₄ seen in the field Y- and T-type brown dwarfs at a few hundred Myr to Gyr ages may have been inherited from the early formation stages. At the density and temperature of Y- and T-type brown dwarfs, it is most likely that the CH₄ observed in their atmosphere has been formed on site, i.e., completely reformed from C and H₂ after the accretion of the gas onto the central part of the proto-BD. Thus, there may not be a direct link between the CH₄ seen in proto-BDs and the one seen in older fully-formed brown dwarfs.

Observations of CH₃D can also be used as a probe of the proto-BD environment, and to investigate whether CH₃D formed on grain surface and evaporated back to the gas-phase, or did it form in the warm $\sim 20\text{--}30$ K regions relatively close to the central object (e.g., Womack et al. 1996; Sakai et al. 2012; Roueff et al. 2013; Asvany et al. 2004; Cleeves et al. 2016; Qasim et al. 2020; Gärtner et al. 2010).

Our IRAM 30 m observations are presented in Sect. 2 and the results thus obtained are presented in Sect. 3. Section 4 presents the formation pathway for the CH₃D and CH₄ molecules in the

* E-mail: briaz@usm.lmu.de

gas- and grain-phase, and Section 5 investigates the possibility of the Warm Carbon Chain Chemistry (WCCC; Sakai et al. 2008) scenario in these cool, dense objects.

2 TARGETS, OBSERVATIONS, AND DATA REDUCTION

We observed the $J_K = 1_0-0_0$ line (232.644301 GHz, Womack et al. 1996) of CH_3D towards the complete sample of 16 Class 0/I proto-BDs described in Riaz & Thi (2022). The observations were obtained at the IRAM 30 m telescope in December, 2017, and February, 2019. We used the EMIR heterodyne receiver (E230 band), and the FTS backend in the wide mode, with a spectral resolution of 200 kHz ($\sim 0.3 \text{ km s}^{-1}$ at 232 GHz). The observations were taken in the frequency switching mode with a frequency throw of approximately 7 MHz. The source integration times ranged from 3 to 4 hours per source per tuning reaching a typical RMS (on T_A^* scale) of $\sim 0.01-0.02$ K. The telescope absolute RMS pointing accuracy is better than $3''$ (Greve et al. 1996). All observations were taken under good weather conditions ($0.08 < \tau < 0.12$; PWV < 2.5 mm). The absolute calibration accuracy for the EMIR receiver is around 10% (Carter et al. 2012). The telescope intensity scale was converted into the main beam brightness temperature (T_{mb}) using standard beam efficiency of $\sim 59\%$ at 230 GHz. The half power beam width of the telescope beam is $\sim 10''$ at 230 GHz. The spectral reduction was conducted using the CLASS software (Hily-Blant et al. 2005) of the GILDAS facility¹. The standard data reduction process consisted of averaging multiple observations, extracting a subset around the line rest frequency, and fitting a low-order (4-6) polynomial baseline which was then subtracted from the average spectrum. We chose a range of ± 10 km/s around the source V_{LSR} to fit the baseline.

At present, reaching the same level of sensitivity of $\sim 10-20$ mK, there are only three proto-BDs in our sample of 16 objects that show a $\geq 3\text{-}\sigma$ detection in CH_3D : SSTc2d J163143.8-245525 (J163143; $L_{\text{bol}} \sim 0.08 L_{\odot}$), SSTc2d J182844.8+005126 (J182844; $L_{\text{bol}} \sim 0.04 L_{\odot}$), and SSTc2d J182959.4+011041 (J182959; $L_{\text{bol}} \sim 0.008 L_{\odot}$). A detailed discussion on the classification and mass and luminosity measurements for these objects can be found in Riaz et al. (2018) and Riaz & Thi (2022).

3 RESULTS

Figure 1 shows the CH_3D spectra for the three proto-BDs. We have measured the parameters of the line center, line width, the peak and integrated intensities using a single-peaked Gaussian fit. The apparent double-peak shape could be due to the noise in the spectrum. The line parameters are listed in Table 1. The uncertainty is estimated to be $\sim 20\%$ for the peak and integrated intensities and Δv , and $\sim 0.02-0.04$ km/s for V_{LSR} . The errors on the line parameters are due to uncertainties in fitting the line profile, and mainly arise from the end points chosen for the Gaussian fit.

As a check, we have compared the CH_3D V_{LSR} with those measured from the C^{17}O (2-1) observations (Riaz et al. 2019). The C^{17}O line is optically thin and provides a reliable reference for the source V_{LSR} . The C^{17}O V_{LSR} is 4.6 ± 0.02 km/s for J163143, 7.8 ± 0.02 km/s for J182844, and 8.4 ± 0.02 km/s for J182959. The C^{17}O V_{LSR} for J163143 and J182959 are consistent with those measured for the CH_3D lines, while a shift of ~ 0.3 km/s is seen for J182844. This shift is likely due to the broad, non-Gaussian shape of the CH_3D profile

for J182844 compared to the Gaussian-like C^{17}O line. Note that the CH_3D FWHM is twice that of C^{17}O for J182844, and the shift in V_{LSR} is within the FWHM.

We had also obtained in the same observing runs spectra at four offset positions around these targets. The off-source spectra were taken at a step size of 1-2 beamsize ($\sim 10''$) offset from the target position. There is no detection in the CH_3D line at a $\geq 2\text{-}\sigma$ level ($1\text{-}\sigma$ rms $\sim 10-20$ mK) at any offset position. We can therefore be confident that the observed CH_3D emission has an origin from the source position. There could still be foreground/background contamination within the beamsize in the on-source spectrum but we cannot quantify it at present without interferometric observations.

The column density of CH_3D is derived from the integrated line intensity by assuming optically thin emission, local thermodynamic equilibrium (LTE) condition, and excitation temperatures of 10 K, 15 K, 20 K, and 25 K. The method for deriving the CH_3D column density is described in the Appendix. The kinetic temperature is expected to be relatively low (~ 10 K) throughout the outer and inner envelope layers in the proto-BDs (e.g., Machida et al. 2009) with only the innermost (< 20 au) region to be at higher temperatures (> 20 K).

The CH_3D column densities and the molecular abundances relative to H_2 , $[N(X)/N(\text{H}_2)]$ are listed in Table 2. The H_2 column densities are computed using the source size and the (dust + gas) mass derived from the sub-millimeter continuum emission (Riaz et al. 2018). The CH_3D and CH_4 abundances for the proto-BDs are higher by a small factor of ~ 1.6 for an excitation temperature of 25 K compared to 10 K (Table 2). Also listed in Table 2 are the CH_4 abundances that were derived from $[\text{CH}_3\text{D}]$ and the $\text{DCO}^+/\text{HCO}^+$ ratios for the proto-BDs (Riaz & Thi 2022). The error on the column densities is propagated from the error on the integrated line intensity, and is estimated to be $\sim 20\%$. The error on the CH_3D abundances is propagated from the error on the CH_3D and H_2 column densities, and is estimated to be $\sim 23\%-24\%$. The error on the CH_4 abundances is propagated from the error on the CH_3D abundance and the D/H ratio, and is estimated to be $\sim 30\%-32\%$.

4 CH_4 AND CH_3D FORMATION PATHWAYS

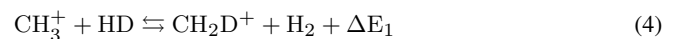
Figure 2 shows the potential gas and surface formation pathways for CH_4 and CH_3D . The cold gas deuteration reactions via H_2D^+ are discussed in Riaz & Thi (2022). The gas-phase formation pathway for CH_3D and CH_4 is initiated by the reaction between C^+ and H_2 (e.g., Roueff et al. 2013; Cleeves et al. 2016; Asvany et al. 2004):



CH_3^+ reacts with H_2 via the slow radiative association reaction:



or can exchange a deuteron atom with HD:



The rate coefficient of reaction (3) decreases with increasing temperature (KIDA database: Wakelam et al. 2012, <http://kida.astrophy.u-bordeaux.fr>). Since the forward reaction (4) is exothermic (with δE_1 between 483 and 660 K depending on the ortho-para ratio of CH_3^+ and H_2 , Roueff et al. 2013), it is in general favoured in the temperature range up to 80 K (Albertsson et al. 2013). However, because the exothermicity is lower for ortho- H_2 , the reverse reaction becomes

¹ <http://www.iram.fr/IRAMFR/GILDAS>

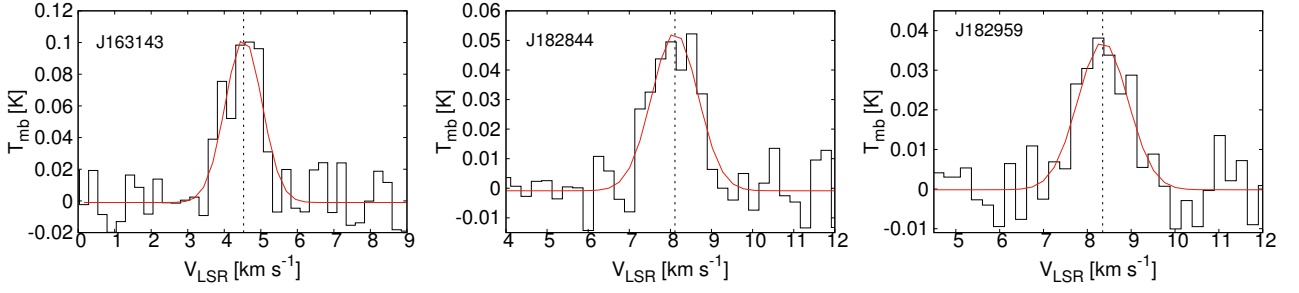


Figure 1. The observed CH₃D spectra (black) with the Gaussian fits (red). Black dashed line marks the cloud systemic velocity of ~ 8 km/s in Serpens and ~ 4.4 km/s in Ophiuchus.

Table 1. CH₃D Line Parameters

Object	V_{lsr} (km s ⁻¹)	T_{mb} (K)	$\int T_{\text{mb}} dv$ (K km s ⁻¹)	Δv (km s ⁻¹)
J163143	4.53±0.02	0.13±0.02	0.13±0.02	1.01±0.24
J182844	8.11±0.03	0.07±0.01	0.08±0.01	1.12±0.25
J182959	8.35±0.02	0.05±0.01	0.06±0.01	1.14±0.25

^a The line parameters have been derived from a single-gaussian fit to the profiles.

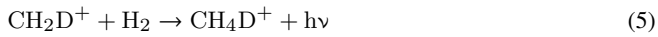
Table 2. Column Densities and Molecular Abundances

Object	N_{H_2} ($\times 10^{22}$ cm ⁻²)	D/H ^a	$N(\text{CH}_3\text{D})$ ($\times 10^{16}$ cm ⁻²) ^b				[CH ₃ D] ($\times 10^{-7}$) ^b				[CH ₄] ($\times 10^{-5}$) ^b			
			10 K	15 K	20 K	25 K	10 K	15 K	20 K	25 K	10 K	15 K	20 K	25 K
J163143	1.8±0.2	0.03±0.006	1.6	1.8	2.1	2.6	8.7	9.9	12.2	14.5	2.9	3.3	4.0	4.8
J182844	3.6±0.5	0.6±0.1	0.8	1.0	1.2	1.4	2.4	2.8	3.3	4.0	0.04	0.04	0.05	0.06
J182959	4.5±0.5	0.4±0.09	0.6	0.7	0.9	1.0	1.4	1.7	1.9	2.3	0.03	0.04	0.04	0.05

^a The [DCO⁺/HCO⁺] ratios are from Riaz & Thi (2022).

^b The errors are estimated to be $\sim 20\%$ on the column densities, $\sim 23\%$ - 24% on the CH₃D abundances, and $\sim 30\%$ - 32% on the CH₄ abundances.

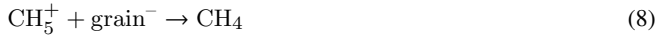
possible at lower temperatures when H₂ is mostly in the ortho state. Similar to CH₃⁺,



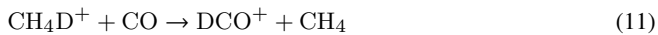
the recombination reaction with free electrons



or on negatively-charged grain surfaces



results in CH₄ and CH₃D. Reaction with CO can lead to HCO⁺ and DCO⁺:



Apart from the two radiative association reactions, the reactions involve an ion and a neutral species and proceed at Langevin rate. The rates are of the order of 10^{-10} - 10^{-9} cm³/s and are temperature-independent. If the grain temperature is below the desorption temperature of ~ 25 K (Collings et al. 2004), CH₄/CH₃D will freeze-out with a typical timescale of ~ 3000 yrs at 10 K and density of 10^6 cm⁻³.

Alternatively, CH₄ and CH₃D can be desorbed from CH₄(ice) and CH₃D(ice) formed on grain surfaces. The formation of CH₄ on ice grains is via successive H or D additions of carbon on grain surfaces (e.g., Qasim et al. 2020). At each stage, it is a competition between attaching H(ice) or D(ice). Once formed, CH₄(ice) does not react with HD or D atom to form CH₃D(ice) due to the endothermicity of the substitution reaction or the existence of barrier (e.g. Li et al. 2015), respectively.

5 DISCUSSION

The main gas-phase channels for the formation of CH₃D and CH₄ is initiated by the formation of CH₅⁺ and CH₄D⁺ via the radiative association reactions (3) and (5), which are enhanced at high densities of 10^8 - 10^{10} cm⁻³ (Cleeves et al. 2016), because the competing electron recombination reactions are hampered by low electron fractions. The ionization rate is proportional to the gas density, while the rate of recombination with electrons depends on the square of the density making the electron density at high densities very low. The reactions are more efficient at low and moderate temperatures ($T < \sim 40$ K).

The detection of CH₃D suggests therefore that we may be probing the innermost densest regions of a proto-BD, close to the jet launching points (< 20 au), where the densities are $\geq 10^8$ cm⁻³ and the temperature can reach values of ~ 20 - 30 K (Machida et al. 2009).

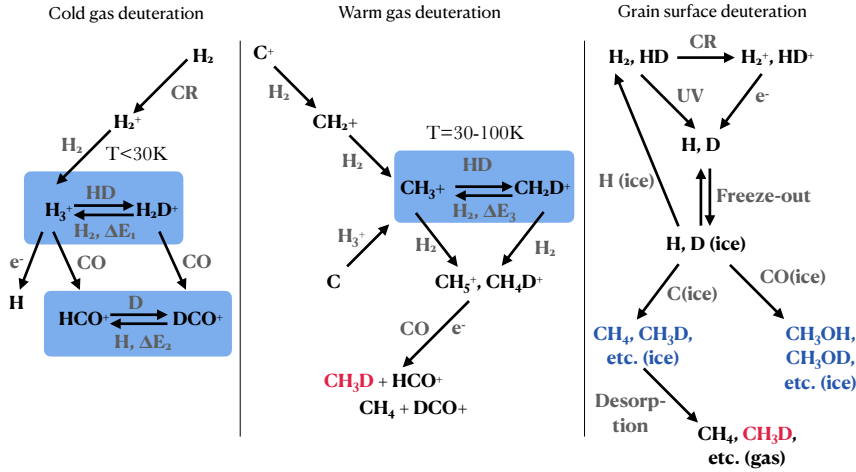


Figure 2. A diagram of the formation pathways for CH_3D and CH_4 via gas-phase and grain surface reactions. $\Delta E_1, E_2, E_3$ are positive (i.e. the reactions are exothermic). Diagram is based on the reactions proposed by Roueff et al. (2013), Albertsson et al. (2013), Cleves et al. (2016), Asvany et al. (2004), and Adams & Smith (1985).

In addition to the gas-phase formation, thermal (when the dust temperature is above 25 K) and/or non-thermal desorption can also return the CH_3D and CH_4 molecules formed on grain surfaces at an earlier evolutionary stage to the gas phase. The abundances for proto-BDs in Table 2 are comparable to the CH_3D ($\sim 3 \times 10^{-7}$) and CH_4 ($\sim 4 \times 10^{-6}$) abundances reported by Sakai et al. (2012) for the low-mass protostar IRAS04368+2557 in L1527. Therefore a Warm Carbon Chain Chemistry may occur in proto-BDs with carbon-chain molecule formation in a lukewarm (~ 20 -30 K) region close to the central proto-BD, similar to the low-mass protostars (Sakai et al. 2008; 2009; 2012).

The proto-BD J163143 (ISO-OPH 200) has been modelled in details by Riaz & Machida (2021). Non-thermal desorption is most likely at play for J163143, which drives a strong jet/outflow. This proto-BD shows a factor of 3-4 higher CH_3D abundance and about 2 orders of magnitude higher CH_4 abundance than the other two proto-BDs. Interestingly, this proto-BD also has a D/H ratio that is about an order of magnitude lower than the other two proto-BDs (Table 2 and Riaz & Thi 2022). There may be a possible dependency between the WCCC and a low deuterium fractionation, as already noted for the case of the low-mass protostar IRAS04368+2557 (Sakai et al. 2012). ISO-OPH 200 is a proto-BD with a very young kinematic age of ~ 6000 yr, and as discussed in Riaz & Machida (2021), the embedded lifetime appears shorter for proto-BDs compared to low-mass protostars, with an earlier transition from the Class 0/I to the Class II phase at < 0.05 Myr rather than ~ 0.1 -0.5 Myr as typically seen for low-mass protostars. A short embedded phase will lower the formation efficiency of molecules on grain surfaces. If indeed we have a case of fast core contraction, then carbon atoms depleted onto dust grains will react with H via grain surface reactions to form $\text{CH}_4(\text{ice})$ before they are converted to CO in the gas phase (e.g., Sakai et al. 2008; 2009). A short embedded life would also imply that the timescale for core contraction is not long enough for deuterium transfer reactions to occur. Together, these scenarios could explain the high CH_3D and CH_4 abundance and low D/H ratio for ISO-OPH 200. Another point to note is the lack of CCS and HC_3N detection in these proto-BDs (Riaz et al. 2018; 2019), which is also consistent with the WCCC scenario (e.g., Sakai et al. 2008).

The lack of detection in CH_3D at a > 2 - σ level for the remaining 13/16 proto-BDs can either be due to the poor line sensitivity of the

observations or the absence of a warm source close to the central proto-BD, such as a high velocity jet, which can warm up the central region and result in the photoevaporation or cosmic-ray-induced evaporation of CH_4 and trigger WCCC. Most of methane and CH_3D molecules in these proto-BDs may still be in the ice form.

Observations of the $J_K = 2_0 - 1_0$ and $J_K = 2_1 - 1_1$ lines at 465 GHz will secure the detection and confirm that the emitting gas is warm. Detection of carbon-chain molecules in the proto-BD with detected CH_3D will test that WCCC occurs in the innermost region of proto-BDs. Finally, sensitive interferometric observations will help to understand the spatial distribution of these molecules and their origin of emission.

ACKNOWLEDGEMENTS

We thank the anonymous referee for several insightful comments on the paper. B.R. acknowledges funding from the Deutsche Forschungsgemeinschaft (DFG) - Projekt number RI-2919/2-1. This work is based on observations carried out with the IRAM 30 m telescope. IRAM is supported by INSU/CNRS (France), MPG (Germany) and IGN (Spain).

6 DATA AVAILABILITY

The data underlying this article are available in the IRAM archives through the VizieR online database.

REFERENCES

- Adams N. G., Smith D., 1985, *ApJL*, 294, L63
 Albertsson T., Semenov D. A., Vasyunin A. I., Henning T., Herbst E., 2013, *ApJS*, 207, 27
 Asvany O., Schlemmer S., Gerlich D., 2004, *ApJ*, 617, 685
 Carter M., Lazareff B., Maier D., Chenu J.-Y., Fontana A.-L., Bortolotti Y., Boucher C., et al., 2012, *A&A*, 538, A89
 Cleves L. I., Bergin E. A., et al., 2016, *ApJ*, 819, 13
 Collings M. P., Anderson M. A., Chen R., Dever J. W., Viti S., Williams D. A., McCoustra M. R. S., 2004, *MNRAS*, 354, 1133
 Cushing M. C., Kirkpatrick J. D., Gelino C. R., et al. 2011, *ApJ*, 743, 50

Endres C. P., Schlemmer S., Schilke P., Stutzki J., Müller H. S. P., 2016, *JMoSp*, 327, 95
 Gärtner S., Krieg J., Klemann A., Asvany O., Schlemmer S., 2010, *A&A*, 516, L3
 Gibb E. L., Rettig T., Brittain S., Haywood R., Simon T., Kulesa C., 2004, *ApJL*, 610, L113
 Greve A., Panis J.-F., Thum C., 1996, *A&AS*, 115, 379
 Hily-Blant P., Teyssier D., Philipp S., Güsten R., 2005, *A&A*, 440, 909
 Kirkpatrick J. D., Gelino C. R., Cushing M. C., et al. 2012, *ApJ*, 753, 156
 Li et al. 2015, *JCP* 142, 204
 Machida M. N., Inutsuka S.-. ichiro ., Matsumoto T., 2009, *ApJL*, 699, L157
 Qasim D., Fedoseev G., Chuang K.-J., et al. 2020, *NatAs*, 4, 781
 Riaz, B.; Thi, W. -F.; Caselli, P., 2018, *MNRAS*, 481, 4662
 Riaz B., Thi W.-F., Caselli P., 2019, *MNRAS*, 483, 1139
 Riaz B. & Bally J., 2021, *MNRAS*, 501, 3781
 Riaz B., Machida M. N., 2021, *MNRAS*, 504, 6049
 Riaz B. & Thi W.-F., 2022, *MNRAS*, *in press*
 Roueff E., Gerin M., Lis D. C., Wootten A., Marcelino N., Cernicharo J., Tercero B., 2013, *JPCA*, 117, 9959
 Sakai N., Sakai T., Hirota T., Yamamoto S., 2008, *ApJ*, 672, 371
 Sakai N., Sakai T., Hirota T., Yamamoto S., 2009, *ApJ*, 702, 1025
 Sakai N., Shirley Y. L., Sakai T., Hirota T., Watanabe Y., Yamamoto S., 2012, *ApJL*, 758, L4
 Townes C. H. & Schawlow A. L., 1975, *Microwave spectroscopy.*, New York, NY (USA): Dover Publications, 698 p.
 Womack M., Apponi A. J., Ziurys L. M., 1996, *ApJ*, 461, 897

This paper has been typeset from a \LaTeX file prepared by the author.

7 APPENDIX

Assuming optically emission, the column density of CH₃D in cm⁻² without correcting for beam dilution effects, is calculated from the line flux of the transition $J_K \rightarrow (J-1)_K$ with $J = 1$ and $K = 0$ using the formula (Womack et al. 1996):

$$N(\text{CH}_3\text{D}) = \frac{3 \times 10^5 \text{k}}{8\pi^3 \nu \mu_0^2} \frac{J}{J^2 - K^2} \frac{Q_{\text{rot}(T_{\text{ex}})} e^{h\nu/kT_{\text{ex}}}}{e^{\Delta E/kT_{\text{rot}}} S_{I,K}} \int T_{\text{mb}} \, d\nu, \quad (12)$$

where ν is the frequency of the transition in Hz (232.6443010 GHz, Womack et al. 1996), μ_0 is the dipole moment in Statcoulomb-centimeters (1 Debye = 10⁻¹⁸ StatC cm), k is the Boltzmann constant (cgs), h is the Plank constant (cgs), J and K are the quantum numbers, T_{ex} is the excitation temperature, T_{rot} is the excitation temperature, $Q_{\text{rot}(T_{\text{ex}})}$ is the partition function at T_{ex} , ΔE is the energy in ergs of the $J-1$ lower level with respect to the ground level, $S_{I,K}$ is the statistical weight factor. T_{mb} is the main-beam temperature in Kelvin and $\int T_{\text{mb}} \, d\nu$ is the line flux in K km s⁻¹. Similar to (Womack et al. 1996), the microwave background was neglected and we assumed $T_{\text{ex}} = T_{\text{rot}}$.

The statistical weight factor is caused by the presence of three equivalent nuclei with $I = 1/2$ (Townes & Schawlow 1975; Womack et al. 1996):

$$S_{I,K} = \frac{2(4I^2 + 4I)}{4I^2 + 4I + 1} \quad (13)$$

The line frequencies, energy levels, and the dipole moment ($\mu_0=0.0059$ Debye) are taken from the CDMS database (Endres et al. 2016). For the $J = 1, K = 0$ transition, $\Delta E = 0$ ergs. The value at T_{ex} of the partition function was calculated using a log-log interpolation of the value in the CDMS database (Endres et al. 2016) instead of an approximate formula. With those values, we reproduced the upper limit from the $J = 2, K = 1$ transition in Womack et al. (1996) within 30%.